

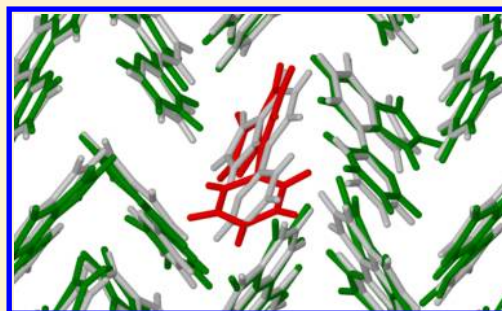
Hybrid QM/QM Simulations of Excited-State Intramolecular Proton Transfer in the Molecular Crystal 7-(2-Pyridyl)-indole

Michael A. Kochman and Carole A. Morrison*

School of Chemistry and EaSTCHEM Research School, The University of Edinburgh, King's Buildings, West Mains Road, Edinburgh, EH9 3JJ, United Kingdom

S Supporting Information

ABSTRACT: A subtractive implementation of the QM/QM hybrid method for the description of photochemical reactions occurring in molecular crystals is presented and tested by applying it in a simulation study of the ultrafast intramolecular excited-state proton transfer reaction in the crystal form of 7-(2-pyridyl)-indole, an organic compound featuring an intramolecular hydrogen bond within a six-membered ring. By propagating molecular dynamics on the excited-state potential energy surface, a mean proton transfer time was calculated as 80 fs. The reaction mechanism is discussed in terms of three-dimensional reaction coordinate diagrams. Proton transfer was found to be barrierless and to be strongly coupled to vibrational modes of the photoexcited molecule that modulate the proton donor–acceptor distance. Some 300 fs after the initial photoexcitation, the excited state molecule reached an S_1/S_0 conical intersection through the mutual twist of the pyridyl and indolyl moieties.



1. INTRODUCTION

Photochemical reactions occurring within molecular crystals are of major importance for their various technological applications, both existing and prospective. Examples include information storage,¹ photoactuators,^{2,3} nonlinear optical materials,⁴ media for optical amplifiers or lasers,⁵ as well as chemical synthesis,^{6,7} including asymmetric synthesis.^{8,9} A distinguishing characteristic of such systems is the interdependence between the reactivity of individual molecules and the bulk crystal structure, which in many cases exerts a strong directing influence and enables clean and controllable photochemical reactions.^{6–9} In computer simulation studies, however, this same feature poses a challenge to the methods of theoretical chemistry. The interplay between crystal architecture and photochemical reactivity necessitates that the simulation method be capable of simultaneously modeling the excited-state process and the interaction of the excited molecule with the surrounding bulk lattice.

The fact that molecular crystals are composed of discrete, relatively weakly interacting molecular units points naturally toward hybrid simulation schemes in which it is assumed that the electronic excitation is localized to a single molecule (or site within a molecule), and the excited molecule and the surrounding bulk lattice are described at different levels of theory.¹⁰ Indeed, studies hybridizing a quantum mechanics (*ab initio* or semiempirical) description of the photoexcited molecule and a molecular mechanics treatment of the surrounding lattice (QM/MM) have previously been reported in the literature.^{11,12}

In the present work, a somewhat different hybrid simulation method is applied, whereby the photoexcited molecule is

treated at the time-dependent DFT (TD-DFT) level with a localized basis set, while the bulk lattice is modeled using the plane-wave DFT approach. In this manner, the potential energy surface is constructed entirely using *ab initio* methods, without recourse to parametrization against experimental data. In order to test the accuracy and predictive power of this hybrid QM/QM simulation method, we have applied it to a model system of an organic crystal whose constituent molecules undergo intramolecular proton transfer on irradiation with UV light. To the best of our knowledge, this is the first attempt to model a photochemical reaction in a molecular crystal using a combination of two quantum mechanical electronic structure methods.

Our motivation in developing this methodology is in part to provide a generally applicable *ab initio* based simulation scheme that is complementary to time-resolved diffraction studies of photochemical reactions within molecular crystals. The model of a solid-state phototochemical reaction implicit in the hybrid QM/QM method, whereby individual photoexcited molecules are surrounded by nonreactive lattice molecules, is an adequate representation of the conditions typically encountered in diffraction experiments, where only a small fraction of molecules comprising the crystal lattice are excited by the pump pulse, and the sample retains its large-scale crystal structure. Hence in order to pave the way for future applications of the hybrid QM/QM method, ample consideration is given here to its practical aspects, such as the validity

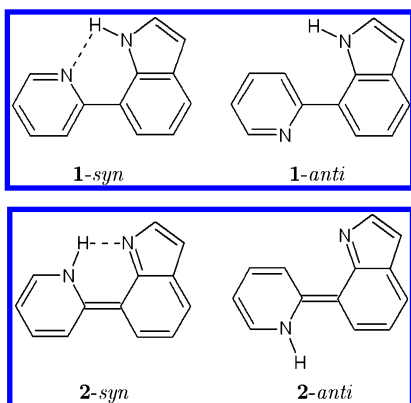
Received: September 17, 2012

Published: January 17, 2013

of the underlying approximations and the accuracy of the component model chemistries.

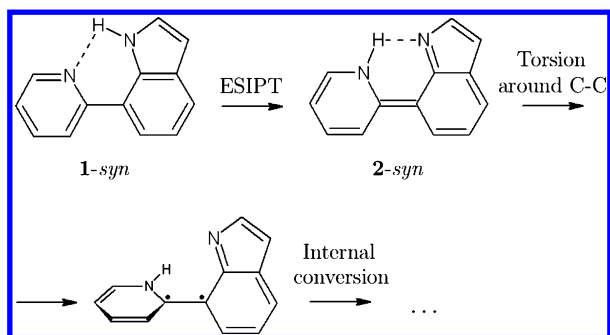
2. MODEL SYSTEM

7-(2-Pyridyl)-indole (abbreviated 7PyIn) is a member of a broad class of Schiff bases which upon irradiation undergo excited-state intramolecular proton transfer (ESIPT) reactions within a hydrogen bond involved in a six-membered ring. In the ground electronic state, the global potential minimum of 7PyIn is the *syn* conformer (hereafter labeled **1-*syn***) in which the shuttling proton is at the indolyl group nitrogen. The *anti* conformer (**1-*anti***) is higher in energy. The *syn* geometry in which the shuttling proton is at the pyridyl group nitrogen (**2-*syn***) is not a minimum on the ground-state potential energy surface according to calculations performed at both the both MP2¹³ and DFT (see section 3.2) levels.



The lowest singlet excited state (S_1) of 7PyIn is an optically bright π,π^* state,¹³ in which the pyridyl group nitrogen is more basic relative to the indolyl group nitrogen. As a result of this change, following photoexcitation to the π,π^* state the proton is transferred from the indolyl group nitrogen to the pyridyl group nitrogen (Scheme 1). Born–Oppenheimer molecular

Scheme 1



dynamics^{14,15} and wavepacket dynamics¹⁶ simulations of ESIPT in related Schiff bases point toward ultrafast proton transfer time scales of around 30–50 fs in the isolated molecules.

In gas phase and solution¹⁷ environments, following proton transfer, the photoexcited 7PyIn molecule undergoes internal conversion (radiationless decay) to the ground state by passing through a conical intersection (CI) between the S_0 and S_1 states, which is reached through a torsional motion around the carbon–carbon bond connecting the pyridyl and indolyl groups. In the vicinity of the conical intersection, where the pyridyl and indolyl groups are at a near-right angle to one

another, the 7PyIn molecule is an almost perfect biradical.¹³ The final products of the internal conversion step have not been determined experimentally but may be expected to consist of a mixture of **1-*syn*** and **2-*anti***. A sketch of the molecular potential energy surface underlying these processes is given in Figure 1.

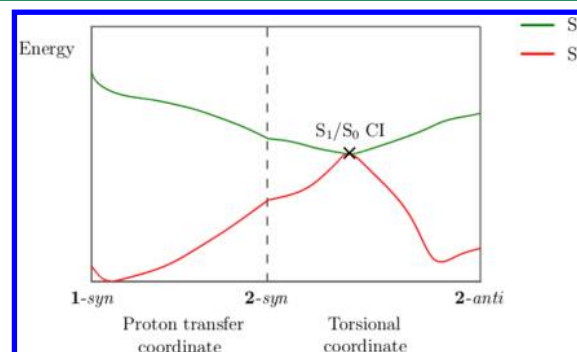
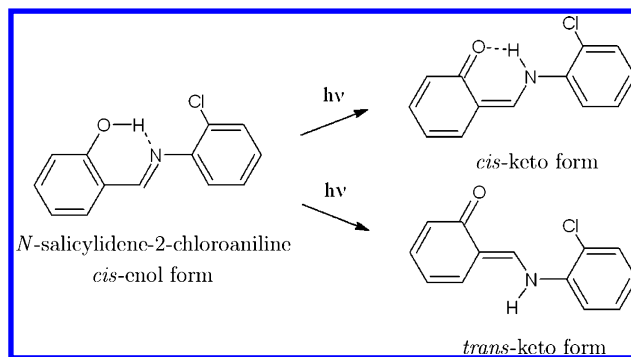


Figure 1. Schematic diagram of the potential energy surface of the 7PyIn molecule along the proton transfer and torsional reaction coordinates, based on the CC2 calculations reported in ref 13.

The photoreactivity pattern outlined above, whereby ESIPT is followed by a twist of the molecular skeleton and internal conversion to the ground state, is also characteristic of many other Schiff bases that undergo ESIPT reactions, including *N*-salicylideneaniline, *N*-salicylidene-2-chloroaniline, and 2-(2'-hydroxyphenyl)benzothiazole. In the molecular crystal forms of some of these compounds, however, the skeletal twisting is prevented by the close packing of molecules in the crystal lattice. For example, in the crystal structure of 2-(2'-hydroxyphenyl)benzothiazole,¹⁸ molecules are planar and π -stacked, leaving no room for torsion around the carbon–carbon bond connecting the benzothiazole and hydroxyphenyl groups.¹⁹ On the other hand, in one of the known polymorphs of *N*-salicylidene-2-chloroaniline,²⁰ molecules do not engage in π -stacking interactions, and the salicylidene and chloroaniline moieties are twisted relative to one another. Owing to the less crowded nature of its crystal structure, irradiation of that *N*-salicylidene-2-chloroaniline polymorph yields the *cis*-keto and, through a pedal motion of the chloroaniline moiety, the *trans*-keto isomers (Scheme 2), with the photoproducts not appearing as a separate crystal phase.²¹ The different coloration of the *trans*-keto and the original *cis*-enol forms is responsible for the photochromic properties of that polymorph. (Another polymorph of *N*-salicylidene-2-chloroaniline exists which

Scheme 2



exhibits π -stacking and is not photochromic.²²) The general rule governing photoisomerization through twisting within molecular crystals of Schiff bases is that less crowded lattices with nonplanar molecules and an absence of $\pi\cdots\pi$ interactions enable photoisomerization, while tightly packed structures which exhibit π -stacking prevent it.²¹

The above examples illustrate the interplay between photoreactivity and crystal structure that occurs in ESIPT reactions of Schiff base molecular crystals. Clearly, it is an interesting question whether the QM/QM hybrid method can make any predictions as to whether the crystal structure of 7PyIn permits the photoexcited molecule to twist around the carbon–carbon bond connecting the pyridyl and indolyl groups and thereby reach the S_1/S_0 CI. Accordingly, in addition to calculating the time scale of the ESIPT reaction, the goal of our simulations was to assess whether that conical intersection is accessible in the molecular crystal phase. To the best of our knowledge, the ESIPT reaction and the possible subsequent radiationless decay process in the crystal form of 7PyIn has not been studied experimentally. In the crystal structure of 7PyIn,²⁴ as shown in Figure 2, there are no π -stacking interactions

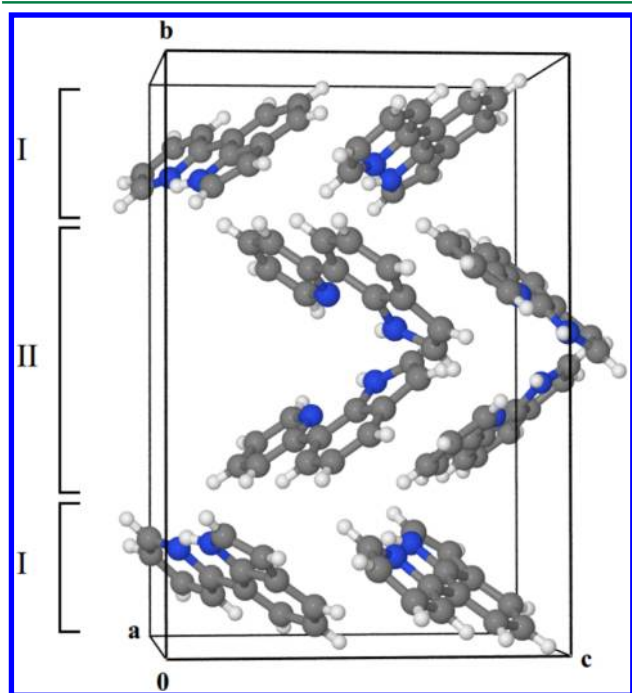


Figure 2. Crystal structure of 7PyIn obtained at $T = 223$ K. The compound crystallizes in orthorhombic space group $Pca2_1$ ²⁵ with two molecules in the asymmetric unit. $a = 9.7196$ Å, $b = 17.4764$ Å, $c = 11.7484$ Å, $Z = 8$. Layers of symmetry-equivalent molecules are labeled I and II.

between molecules, and the density calculated from the crystal cell and contents, at 1.293 g/cm³, is low. Therefore, through comparison with other examples of ESIPT systems,^{21,22} we anticipate that the crystal packing should not prevent the photoexcited molecule from reaching the CI.

We remark here, however, that a single-configurational method such as TD-DFT is incapable of correctly describing the vicinity of a CI, where the wave function has an intrinsic multiconfigurational character, and may also incorrectly predict the electron density distribution for a biradicaloid state, such as the 7PyIn molecule near the CI. It will therefore also be

essential to critically assess the ability of TD-DFT to provide a correct potential energy surface for the twisting motion of 7PyIn.

In several studies of excited-state *cis*–*trans* isomerizations through rotations around double bonds,²³ including in ESIPT systems structurally related to 7PyIn,^{15,16} results obtained using the TD-DFT method in conjunction with various exchange–correlation functionals were benchmarked against those computed with the use of multiconfigurational methods, which are capable of correctly describing conical intersections as well as biradicals. Encouragingly, in each of the works just cited, TD-DFT was found to correctly predict the existence and rough location of the relevant conical intersection, in that in the vicinity of the CI the energy separation between the ground state and the first singlet excited state became small. We are also unaware of any report of TD-DFT giving rise to a qualitatively incorrect description of an ESIPT system.

In the case of 7PyIn, as explained in section 4.1, by comparing potential energy surface scans at the TD-DFT and the Complete Active Space SCF (CASSCF) levels, we have obtained results in line with the current literature norms, in that although TD-DFT does appear to qualitatively predict the existence of the relevant CI in 7PyIn, the exact location of the CI and the topology of the potential energy surface around it may be somewhat in error. Despite this, in view of the vastly superior computational efficiency offered by TD-DFT as compared to multiconfigurational methods, as well as its ability to predict ESIPT time scales in agreement with experimental data,¹⁶ in the hybrid QM/QM scheme applied in the present work, we have used the TD-DFT method to describe the photoexcited molecule. The possible error resulting from the use of the TD-DFT method was quantified by comparing with CASSCF calculations and was borne in mind when interpreting the simulation results.

A point of note is that the asymmetric unit of the 7PyIn crystal consists of two molecules, which form alternating double layers parallel to the *ac* plane (labeled I and II in Figure 2). Molecules within each layer type are equivalent by the symmetry of the crystal structure. As the local environments of molecules occupying the two different symmetry sites are different, when conducting molecular dynamics simulations of ESIPT, we have selected molecules to photoexcite from among molecules of both symmetry types.

3. COMPUTATIONAL METHODS

3.1. Outline of Simulation Scheme. In the present section, we sketch out the computational procedure that was used to study the ESIPT reaction in the crystal lattice of 7PyIn, assuming that one molecule out of eight within the unit cell undergoes photoexcitation.

1. First, geometries of the 1-*syn* and 1-*anti* conformers of the 7PyIn isolated molecule were optimized at the DFT level of theory. Vertical excitation energies were calculated using the TD-DFT method.

2. A relaxed potential energy scan along the torsion angle formed by the atoms C1–C2–C3–N2 (henceforth denoted as ϕ , see Figure 3a in section 4.1 for atom numbering), which describes rotation around the carbon–carbon bond connecting the pyridyl and indolyl moieties, was carried out for the 2-*syn* tautomer on the S_1 potential energy surface at the TD-DFT level. Energies of points along the torsional coordinate were subsequently recalculated at the CASSCF level.

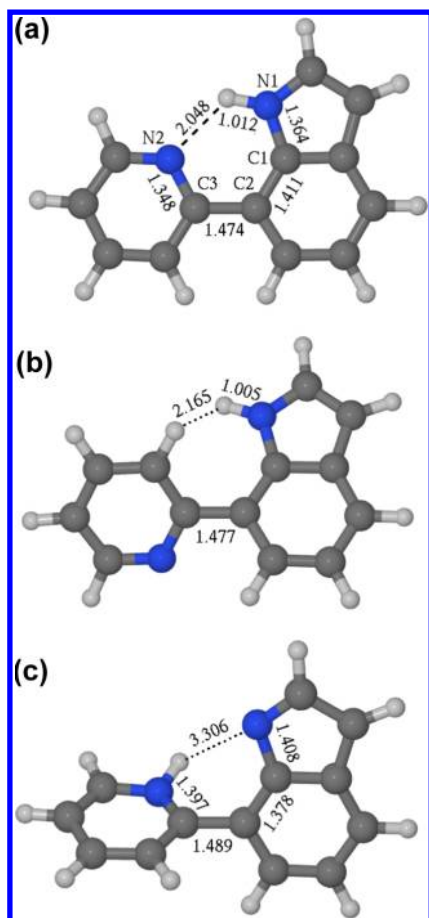


Figure 3. Geometries of the 7PyIn molecule. All distances are given in units of Å. (a) 1-*syn* conformation optimized at the PBE0/6-31G(d,p) level, $\phi = 0.0^\circ$. (b) 1-*anti* conformation, optimized at the PBE0/6-31G(d,p) level, $\phi = 148.2^\circ$. (c) S_1/S_0 conical intersection located at the SA-2-CASSCF(6,6) level.

3. A unit cell of the 7PyIn crystal, representing the bulk lattice, was thoroughly equilibrated by means of MD simulation in the canonical ensemble on the ground-state potential energy surface.

4. Phase space points (i.e., sets of atomic coordinates and velocities) were sampled from the production run at long time intervals.

5. For each selected phase space point, photoexcitation to the S_1 state of a single molecule of 7PyIn embedded in the crystal lattice was modeled by taking the system from the ground-state DFT potential energy surface to a hybrid QM/QM excited-state potential energy surface in which the photoexcited molecule is treated using the TD-DFT method, while the remaining molecules are described using ground-state DFT.

6. For each such photoexcited system, molecular dynamics was propagated in the microcanonical ensemble on the hybrid QM/QM potential energy surface. The progress of the ESIPt reaction and subsequent skeletal twisting of the photoexcited 7PyIn molecule was monitored by following structural parameters such as the proton transfer coordinate and the donor–acceptor distance.

The various components of the simulation are described in detail in the following subsections.

3.2. The QM/QM Hybrid Method. The mathematical framework for using different levels of theory to describe distinct regions of a chemical system is provided by the QM/

MM method, which was originally introduced by Warshel and Levitt²⁶ for the simulation of enzymatic reactions. In this formulation of QM/MM, the active site was described by means of a quantum-mechanical (QM) electronic structure method while the remainder of the system was treated using a classical molecular mechanics (MM) force field. Since this pioneering study, the QM/MM method has been developed extensively and applied to a broad range of problems,^{27,28} including excited-state systems in which the electronic excitation was considered to be localized in one part of a larger system.^{11,12,29,30} In a relatively small number of studies,^{31–37} both the reaction site and the rest of the system have been treated using different QM methods; this variant is usually termed QM/QM. In the present work, we take this approach to perform a simulation of a photochemically induced proton transfer reaction and subsequent internal conversion through a CI for the 7PyIn molecular crystal, treating the electronic excitation as localized to a single molecule embedded within the crystal lattice.

The reactive molecule is described using the TD-DFT method with a localized basis set while the nonreactive molecules which represent the bulk lattice are treated using DFT with a plane-wave basis set. This TD-DFT/DFT hybrid computational scheme is described in detail in the following subsection.

3.3. Definition of System Energy. The QM/QM method used in the present work is defined formally by the following expression for the total energy of the simulated system, which is an adaptation of the subtractive QM/MM scheme²⁷ to the combination of the TD-DFT and DFT methods:

$$E_{\text{TD-DFT/DFT}}(\mathbf{S}) = E_{\text{DFT}}^{\text{PW}}(\mathbf{S}) + E_{\text{TD-DFT}}^{\text{GTO}}(\mathbf{C}) - E_{\text{DFT}}^{\text{PW}}(\mathbf{C}) \quad (1)$$

where \mathbf{S} denotes the entire system including the photoexcited molecule and \mathbf{C} , the photoexcited molecule alone. The subscripts TD-DFT and DFT refer to the electronic structure methods, whereas the superscripts PW (plane wave) and GTO (Gaussian-type orbital) refer to the basis sets used for the evaluation of the respective terms.

The term $E_{\text{DFT}}^{\text{PW}}(\mathbf{S})$ represents the potential energy of the entire system evaluated through a periodic DFT calculation and includes all interactions between the photoexcited molecule and the surrounding bulk lattice. As such, these interactions are treated purely at the DFT level, as though the reactive molecule was in the electronic ground state, which is an approximation of the subtractive QM/MM scheme.

$E_{\text{TD-DFT}}^{\text{GTO}}(\mathbf{C})$ and $E_{\text{DFT}}^{\text{PW}}(\mathbf{C})$ are the potential energies of the reactive molecule alone, evaluated respectively at the TD-DFT and DFT levels in the absence of the surrounding periodic lattice. $E_{\text{TD-DFT}}^{\text{GTO}}(\mathbf{C})$ is calculated using a localized (Gaussian-type orbital) basis set. Since this term is calculated as though the reactive molecule was removed from the periodic lattice, within the TD-DFT calculation the reactive molecule does not experience the polarizing influence of the surrounding crystal lattice, which is another approximation inherent in the subtractive QM/MM scheme.

The term $E_{\text{DFT}}^{\text{PW}}(\mathbf{C})$ is subtracted from the sum $E_{\text{DFT}}^{\text{PW}}(\mathbf{S}) + E_{\text{TD-DFT}}^{\text{GTO}}(\mathbf{C})$ in order to correct for the double counting of the intramolecular energy of the reactive molecule at the ground-state DFT level. It is evaluated at the same level of theory as $E_{\text{DFT}}^{\text{PW}}(\mathbf{S})$, except that in the term $E_{\text{DFT}}^{\text{PW}}(\mathbf{C})$ the reactive molecule \mathbf{C} is treated as an isolated system.

Because of the above-mentioned approximations intrinsic to the subtractive QM/MM scheme, within the present implementation of the QM/QM hybrid method the electronic structure of the photoexcited molecule is calculated as though it were an isolated molecule. Hence, excitation energies calculated within the present QM/QM hybrid method are not accurate in the absolute sense, as they do not account for the polarization of the excited molecule by the crystalline environment. However, provided that electrostatic interactions between the excited molecule and the surrounding crystal lattice are reasonably weak, the energetic order of electronic states at a given nuclear geometry will not be affected by these interactions. In the case of 7PyIn, by carrying out a simple embedded cluster calculation of a 7PyIn molecule surrounded by a system of point charges representing the bulk lattice, we have verified that the energies of the five lowest singlet excited states and the dipole moment of the 7PyIn molecule in the S_1 electronic state are only slightly affected by polarization by the surrounding lattice. The details of this calculation are described in the Supporting Information. Thus, we believe that the approximation made by neglecting the polarization of the photoexcited molecule by the surrounding bulk lattice in the TD-DFT calculation is very unlikely to give rise to significant error in this case.

Furthermore, as long as the electron density differences between the ground and the relevant excited states are small, we believe that it is a justifiable approximation to evaluate interactions between the excited molecule and the surrounding lattice as though both were in the electronic ground state. In conclusion, provided that molecules comprising the simulated system are not strongly polar, and that the relevant excited state is not a charge-transfer state, we expect that the present QM/QM hybrid method is able to construct a realistic potential energy surface, in the sense that differentiation of eq 1 with respect to nuclear coordinates will yield realistic forces.

3.4. Simulation Setup. **3.4.1. Isolated-Molecule Calculations.** Geometry optimizations of the isolated 7PyIn molecule were carried out using the PBE0³⁸ exchange-correlation functional with the 6-31G(d,p) basis set as implemented in the computational chemistry software package Gaussian 09.³⁹ The default Berny algorithm using GEDIIS in redundant internal coordinates was used in geometry optimization. Vertical excitation energies were calculated for both the 1-*syn* and 2-*syn* tautomers of 7PyIn. Next, a relaxed potential energy surface (PES) scan along the torsion angle ϕ , which describes rotation around the carbon-carbon bond connecting the pyridyl and indolyl moieties, was conducted for the 2-*syn* tautomer on the S_1 potential energy surface using the TD-DFT method. At each scan point, the torsion angle ϕ was constrained while all other redundant internal coordinates were optimized.

Single-point CASSCF calculations at geometries derived from the TD-DFT PES scan were carried out within Gaussian 03.⁴⁰ All calculations were state averaged over the two states of interest (S_0 and S_1) with equal weights. For the starting orbitals for the CASSCF calculations, we have used natural orbitals extracted from an unrestricted Hartree-Fock calculation, carried out with the minimal STO-3G basis set, for the planar structure of the 2-*syn* tautomer obtained from the TD-DFT PES scan. All natural orbitals with occupation numbers in the range 0.05 to 1.95 were included in the active space of an initial CASSCF calculation, leading to an active space comprising eight electrons distributed in eight orbitals, or an (8,8) active

space. All orbitals included in the active space had π -type symmetry. The STO-3G CASSCF wave function was subsequently projected onto progressively larger basis sets up to 6-31G(d), which was used in all production CASSCF calculations. This model chemistry is abbreviated SA-2-CASSCF(8,8). The same active space was carried over to single point calculations for all other structures obtained in the PES scan of the 2-*syn* tautomer.

The geometry with $\phi = 40^\circ$ obtained from the PES scan of the 2-*syn* tautomer was also used as a starting point for a search for the S_1/S_0 conical intersection involved in the *syn* to *anti* photoisomerization of 7PyIn. Because prior calculations at the approximate coupled-cluster singles-and-doubles (CC2) level reported in ref 13 suggest that this CI occurs at a torsion angle $\phi \approx 90^\circ$, it was anticipated that the active space chosen at the planar geometry ($\phi = 0^\circ$) may no longer be suitable for the CI search. Therefore, for the purpose of locating the S_1/S_0 CI, the CASSCF active space was chosen anew at the $\phi = 40^\circ$ geometry. As before, natural orbitals from a UHF/STO-3G calculation were used as the starting orbitals for CASSCF, and all natural orbitals with occupation numbers in the range 0.05 to 1.95 were included in the active space, now giving rise to an active space comprising six electrons distributed among six orbitals. This (6,6) active space contained three predominantly π -type occupied orbitals and three predominantly π -type virtual orbitals. The STO-3G wave function was then projected onto progressively larger basis sets, up to the 6-31G(d) basis set, which was utilized in the CI search. The model chemistry described above will henceforth be denoted as SA-2-CASSCF-(6,6).

3.4.2. Solid State Calculations. In the equilibration of the ground-state 7PyIn crystal unit cell in the ground electronic state, the potential energy of the system was evaluated using the Perdew-Burke-Ernzerhof exchange-correlation DFT functional⁴¹ as implemented in the software package CASTEP, Academic Release version 5.501.⁴² A plane-wave cutoff of 400 eV was applied. The electronic Brillouin zone was sampled by using a Monkhorst-Pack k -point grid with a k -point spacing of at most 0.1 \AA^{-1} , achieved using a single k -point at $(\frac{1}{4} 0 0)$. The default ultrasoft pseudopotentials were used.⁴³ This choice of plane-wave cutoff and maximum k -point spacing represents a compromise between computational efficiency and accuracy. As we will demonstrate in section 4.2, the plane-wave DFT calculation very accurately reproduces the experimental crystal structure, and for that reason this compromise was deemed acceptable. Energies and forces were corrected for dispersion interactions using the semiempirical scheme of Grimme.⁴⁴ The SCF electronic energy convergence criterion was set to $1.0 \times 10^{-7} \text{ eV/atom}$. The same level of theory was applied in the hybrid QM/QM simulations of the photoexcited system when evaluating the term $E_{\text{DFT}}^{\text{PW}}(S)$.

When calculating the term $E_{\text{DFT}}^{\text{PW}}(C)$, the reactive molecule was placed in a cubic supercell of edge length 20 Å, which was found to be large enough that the total energy did not change significantly on increasing the supercell size further. The electronic Brillouin zone was sampled at the Γ -point only. The remaining calculation parameters were identical as in the evaluation of the term $E_{\text{DFT}}^{\text{PW}}(S)$.

The term $E_{\text{TD-DFT}}^{\text{GTO}}(C)$ was evaluated using the PBE0/6-31G(d,p) model chemistry within Gaussian 09,³⁹ with the molecule C in the S_1 electronic state.

The ground-state system was equilibrated by propagating Born-Oppenheimer molecular dynamics in the NVT ensemble

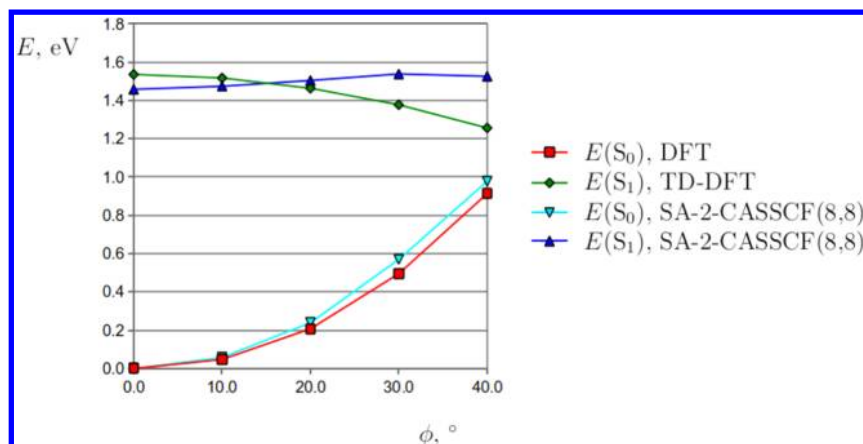


Figure 4. Potential energy surfaces of the 2-*syn* tautomer as a function of the C1–C2–C3–N2 torsion angle (ϕ). The molecular geometries were obtained through a relaxed PES scan on the S_1 surface calculated using the TD–DFT method, in which the torsion angle ϕ was constrained while all other redundant internal coordinates were optimized at each scan point. The DFT S_0 state energy and the SA-CASSCF(8,8) S_1 and S_0 energies were calculated at the geometries extracted from the TD–DFT PES scan. The origin of the energy axis is taken at the ground-state energy of the planar 2-*syn* tautomer.

for 3 ps, following which a production run of 7 ps was carried out. Throughout the equilibration and production periods, the temperature was maintained at 220 K using a chain of five Nosé–Hoover thermostats with a relaxation time of $\tau = 1$ ps. A time step of 1 fs was used throughout the equilibration and production periods. Phase space points were collected from the production run at intervals of 1 ps starting from $t = 3$ ps to serve as starting points for the hybrid QM/QM simulations of ESIPT, for a total of eight starting points. From each starting point, two trajectories were propagated: one in which the photoexcited molecule was selected from among the symmetry type I molecules and another in which it was selected from among the symmetry type II molecules, for a total of 16 trajectories (see Figure 2 and accompanying text for an explanation of the symmetry labels I and II).

The ESIPT reaction was modeled by propagating molecular dynamics in the NVE ensemble on the hybrid QM/QM potential energy surface. Newton's equations of motion were integrated using the Velocity Verlet scheme with a time step of 0.5 fs. On the grounds that previous studies of ESIPT in structurally similar systems have characterized the proton transfer as a ballistic motion of the wave packet, with no significant involvement of proton tunneling,^{45,46} we believe that the treatment of the shuttling proton as a classical point particle did not introduce large error into the simulation of the proton transfer reaction. The dynamics was propagated until the system reached the S_1/S_0 conical intersection, which occurred in every simulated trajectory.

The calculation of the terms $E_{\text{DFT}}^{\text{PW}}(\mathbf{S})$, $E_{\text{TD-DFT}}^{\text{GTO}}(\mathbf{C})$, and $E_{\text{DFT}}^{\text{PW}}(\mathbf{C})$ in the course of MD simulations on the QM/QM potential energy surface, as well as the integration of Newton's equations of motion using the Velocity Verlet algorithm, was managed by a bash “wrapper” script. In each MD iteration, the script created a Gaussian 09 input file for the calculation of the term $E_{\text{TD-DFT}}^{\text{GTO}}(\mathbf{C})$ and CASTEP input files for the calculation of the terms $E_{\text{DFT}}^{\text{PW}}(\mathbf{S})$ and $E_{\text{DFT}}^{\text{PW}}(\mathbf{C})$. The script then successively executed the Gaussian 09 calculation and the two CASTEP calculations and extracted the potential energies and atomic forces from the resulting output file.

The force vector $\mathbf{F}(\mathbf{S}_i) = -((\partial/\partial x_i) + (\partial/\partial y_i) + (\partial/\partial z_i))E(\mathbf{S}) = -\nabla_i E(\mathbf{S})$ on any atom i was calculated as minus the gradient of eq 1 with respect to the Cartesian coordinates of

that atom, resulting in the following expression for the net force:

$$\mathbf{F}(\mathbf{S}_i) = \begin{cases} -\nabla_i E_{\text{DFT}}^{\text{PW}}(\mathbf{S}) - \nabla_i E_{\text{TD-DFT}}^{\text{GTO}}(\mathbf{C}) + \nabla_i E_{\text{DFT}}^{\text{PW}}(\mathbf{C}) & \text{if atom } i \text{ belongs to the photoexcited molecule } \mathbf{C} \\ -\nabla_i E_{\text{DFT}}^{\text{PW}}(\mathbf{S}) & \text{otherwise} \end{cases} \quad (2)$$

where the terms $-\nabla_i E_{\text{DFT}}^{\text{PW}}(\mathbf{S})$, $-\nabla_i E_{\text{TD-DFT}}^{\text{GTO}}(\mathbf{C})$, and $-\nabla_i E_{\text{DFT}}^{\text{PW}}(\mathbf{C})$ are simply the forces on the i th atom obtained from the respective DFT, TD-DFT, and DFT calculations. Owing to the approximations inherent in the subtractive QM/QM scheme, eq 2 is the only stage at which the two model chemistries used in a QM/QM simulation are meshed together.

4. RESULTS AND DISCUSSION

4.1. Energy Minima of the Isolated Molecule.

Equilibrium geometries of the 1-*syn* and 1-*anti* conformers of 7PyIn are presented in Figure 3a and b, respectively. The 1-*syn* conformer adopts a planar geometry that belongs to the C_s point group. In the 1-*anti* conformer, the pyridyl and indolyl moieties are twisted relative to one another, with a torsion angle ϕ (the torsion angle formed by the atoms C1–C2–C3–N2, see Figure 3a for atom numbering) of 148.2°. The 1-*anti* conformer is higher in energy than the 1-*syn* by 0.260 eV (25.1 kJ/mol, energy difference corrected for zero-point vibrational energy). The vertical $S_0 \rightarrow S_1$ excitation energy for the 1-*syn* conformer was calculated as 3.80 eV. A potential energy surface scan along ϕ on the S_1 surface (calculated at the TD-DFT level) was conducted for the 2-*syn* tautomer, in which the proton is located at the pyridyl group nitrogen N2. The torsion angle ϕ was varied in the range 0° to 40° in steps of 10°, and all other redundant internal coordinates were reoptimized at each step. The energy at each resulting point on the PES was subsequently recalculated at the SA-2-CASSCF(8,8) level of theory. The potential energy values along the torsional coordinate calculated using the TD-DFT and SA-2-CASSCF(8,8) methods are compared in Figure 4, which we will now discuss in some detail.

It can be seen from Figure 4 that the DFT and the SA-CASSCF(8,8) methods provide a very similar characterization of the S_0 potential energy surface. Vertical excitation energies of

the planar 2-*syn* conformer calculated at the TD-DFT and SA-CASSCF(8,8) levels are also in good agreement, at 1.536 and 1.458 eV, respectively. However, these two methods paint somewhat different pictures of the topology of the S_1 potential energy surface. At the TD-DFT level, the energy of the S_1 state decreases monotonically with increasing torsion angle ϕ , and the S_0 and S_1 states are very close in energy (0.343 eV apart) at $\phi = 40^\circ$. An attempt to continue the potential energy surface scan to $\phi = 50^\circ$ resulted in failure of the TD-DFT calculation, indicating that the TD-DFT method predicts that the S_1/S_0 conical intersection occurs for a ϕ value just over 40° . In contrast, at the SA-CASSCF(8,8) level the energy of the S_1 state varies more weakly with ϕ , increasing by around 0.08 eV over the range of $\phi = 0^\circ$ to 30° and then decreasing by around 0.01 eV from $\phi = 30^\circ$ to 40° .

The geometry of the S_1/S_0 conical intersection, located at the SA-2-CASSCF(6,6) level, is presented in Figure 3c. At this geometry, the energy gap between S_1 and S_0 states is 0.041 eV (4.0 kJ/mol), and the torsion angle ϕ takes a value of 72.3° . There remains a vestigial hydrogen bond at the conical intersection geometry, as evidenced by the H–N bond within the pyridyl moiety being slightly bent toward the indolyl group nitrogen.

It is difficult to judge which of the TD-DFT and CASSCF methods provides a more reliable description of the S_1 potential energy surface along the torsional coordinate. While the CASSCF method is capable of characterizing both biradicaloid states and conical intersections, it lacks dynamic correlation effects, and furthermore in the present work the CASSCF calculations were carried out in a relatively modest active space and with a fairly limited basis set. Due to these considerations, we do not treat the calculations performed using the CASSCF method as an exact benchmark but merely use them to identify the possible error introduced by employing the TD-DFT method.

Clearly, at the CASSCF level of theory, the S_1/S_0 conical intersection is located at a substantially higher value of ϕ than that suggested by the TD-DFT calculations. Furthermore, the TD-DFT method predicts a different topology of the S_1 potential energy surface than CASSCF. Because at the TD-DFT level the potential energy of the 2-*syn* tautomer in the S_1 state decreases with increasing torsion angle ϕ , we might expect that the photoexcited molecule is funneled toward the S_1/S_0 CI by the topology of the TD-DFT potential energy surface. This effect is absent at the CASSCF level, where the S_1 potential energy surface is flatter, which may result in an artificially strong tendency of the photoexcited molecule in the TD-DFT/DFT hybrid simulations to reach the S_1/S_0 CI. The differences between energies of the S_1 state calculated at the TD-DFT and CASSCF levels are reasonably small, however, up to 0.348 eV for the $\phi = 40^\circ$ structure, relative to the $\phi = 0^\circ$ structure. Also, a survey of trajectories generated on the TD-DFT/DFT potential energy surface, presented in Table 1, shows that in some trajectories, upon reaching the S_1/S_0 CI, the photoexcited molecule adopted an absolute value of ϕ of around $60\text{--}70^\circ$, which coincides closely with the value of 72.3° predicted for the CI at the SA-2-CASSCF(6,6) level. Hence, we believe that although the TD-DFT method may give rise to an incorrect topology of the potential energy surface near the S_1/S_0 CI, it does provide an adequate description of the torsional motion of the photoexcited molecule in the sense that configurations near the S_1/S_0 CI that are reached by trajectories propagated on the

Table 1. Results of Simulated Trajectories on the TD-DFT/DFT Hybrid Potential Energy Surface

excited molecule symmetry type ^a	trajectory	t_{PT} , fs ^b	t_{CI} , fs ^b	$\Delta E(0)$, eV ^c	$\phi(0)$, deg ^d	$\phi(t_{CI})$, deg ^d
I	1	55.5	184.5	3.6764	1.0	−58.0
	2	42.0	174.5	3.6314	14.2	43.6
	3	128.5	386.5	3.8035	−10.5	47.6
	4	55.0	309.0	3.7983	0.6	46.9
	5	90.0	472.5	3.5006	−6.4	38.0
	6	130.0	432.0	3.8134	11.5	54.5
	7	91.0	275.5	3.8254	−7.6	−70.3
	8	142.5	279.0	3.4211	−8.1	41.2
II	1	75.0	374.0	3.6892	−3.4	−49.2
	2	88.0	325.5	3.6444	3.1	54.1
	3	39.5	182.5	3.6872	5.7	42.8
	4	22.0	283.5	3.5532	−8.6	51.9
	5	80.5	335.5	3.6607	14.9	−55.6
	6	108.5	221.0	3.7655	4.9	51.9
	7	91.5	267.0	3.8419	−9.6	40.8
	8	43.5	324.0	3.6108	6.3	−44.2

^aI and II refer to the choice of the excited molecule from among the two molecules within the asymmetric unit. ^b t_{PT} and t_{CI} are respectively the time at which proton transfer occurred and the time at which the photoexcited molecule reached the conical intersection, where $t = 0$ corresponds to the photoexcitation time. ^c $\Delta E(0)$ is the potential energy gap between the states S_1 and S_0 at $t = 0$. ^d $\phi(0)$ and $\phi(t_{CI})$ are respectively the values of the torsion angle ϕ at the time of the initial photoexcitation and on reaching the S_1/S_0 CI.

TD-DFT/DFT hybrid potential energy surface are also energetically accessible to the real system.

4.2. Crystal Structure of 7PyIn. In order to assess the quality of the simulation of the crystal structure of 7PyIn by the ground-state DFT potential energy surface used in the MD calculations, time-averaged atomic positions were extracted from the production MD run. A superposition of the time-averaged crystal structure of 7PyIn onto the experimentally determined structure is shown in Figure 5, where it can be seen

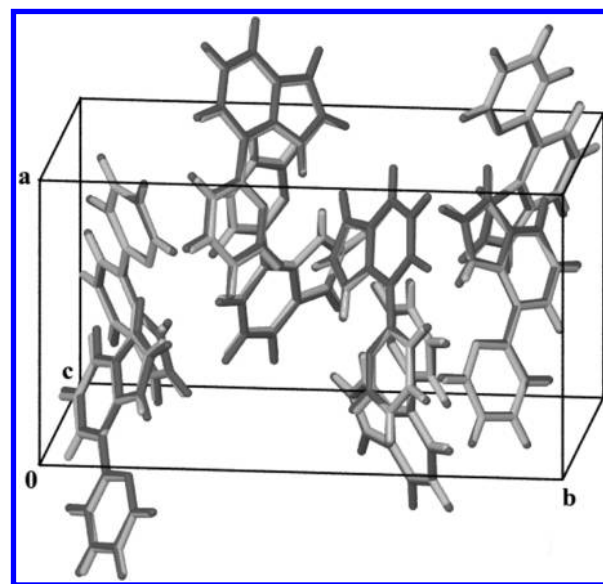


Figure 5. An overlay of the experimental and time-averaged simulated structures of 7PyIn, in light gray and dark gray respectively.

that the time-averaged atomic positions coincide very closely with the experimental positions. Hence, we infer that the model chemistry used in the MD simulations correctly reproduces the crystal structure at the relevant temperature and density.

4.3. Proton Transfer and Accessibility of the S_1/S_0 Conical Intersection. The progress of the excited-state trajectories was followed by monitoring a set of structural and energetic parameters, whose definitions we will now provide. The proton transfer coordinate is defined as the difference between the lengths of the breaking N1–H bond and the forming N2–H bond, $R(\text{N1-H}) - R(\text{N2-H})$. Proton transfer was considered to have occurred at the point when the system passed through the line of $R(\text{N1-H}) - R(\text{N2-H}) = 0$. Although in principle it is possible for the shuttling proton to undergo back transfer from nitrogen N1 to N2, and hence cross through $R(\text{N1-H}) - R(\text{N2-H}) = 0$ multiple times, this did not occur in any of the simulated trajectories. The proton donor–acceptor distance in the ESIPT reaction is denoted $R(\text{N1-N2})$. The potential energy of the system with the reactive molecule in the S_1 state is given by eq 1. Throughout each trajectory, we also followed the ground-state potential energy of the system, which is defined by

$$E(S_0) = E_{\text{DFT}}^{\text{PW}}(\mathbf{S}) + E_{\text{DFT}}^{\text{GTO}}(\mathbf{C}) - E_{\text{DFT}}^{\text{PW}}(\mathbf{C}) \quad (3)$$

Here, $E_{\text{DFT}}^{\text{GTO}}(\mathbf{C})$ represents the ground-state potential energy of the photoexcited molecule, calculated at the PBE0/6-31G(d,p) level of theory. The system was considered to have reached the S_1/S_0 CI when the potential energy gap between the excited and ground states, $\Delta E = E(S_1) - E(S_0)$, decreased to below the arbitrarily chosen threshold value of 0.1 eV.

The results of all 16 simulated trajectories are reviewed in Table 1. Proton transfer occurred in every simulated trajectory, with a mean proton transfer time of 80 fs, indicating a barrierless, or near-barrierless, ESIPT mechanism. In each case, following proton transfer, the photoexcited molecule reached the S_1/S_0 CI, at which point the simulation was terminated because of the inability of TD-DFT to correctly describe the crossing region. We note from the data presented in Table 1 that there is no significant difference in either the mean proton transfer time, or the mean time required for the photoexcited molecule to reach the S_1/S_0 CI, between the two inequivalent molecules within the crystal lattice.

Given that the CI was reached by all simulated trajectories within around 0.5 ps of the initial photoexcitation, it appears that on the hybrid TD-DFT/DFT potential energy surface the twisting motion of the photoexcited 7PyIn molecule within the corresponding crystal lattice is either barrierless or occurs through a potential barrier that is low relative to the kinetic energy of the photoexcited molecule. Hence, on the TD-DFT/DFT potential energy surface both the proton transfer and the internal conversion steps are essentially barrierless, and photoexcited molecules are efficiently funneled toward the CI. In light of the possibly incorrect description of the twisting motion in 7PyIn TD-DFT as discussed in section 4.1, we conclude that our molecular dynamics simulations on the TD-DFT/DFT potential energy surface predict that in the real system, the S_1/S_0 CI is energetically accessible, but the rate and quantum yield of the internal conversion process may both be lower than the very high rate (under 0.5 ps) and 100% quantum yield our simulations would suggest.

We must also point out that the finding that all photoexcited molecules rapidly reach the S_1/S_0 CI does not, on its own, indicate that *syn* to *anti* isomerization occurs in the 7PyIn

crystal, since molecules which pass through the conical intersection may potentially relax to both the *syn* and *anti* forms. However, from the finding that in some simulated trajectories, on reaching the S_1/S_0 CI, the photoexcited molecule had a high absolute value of ϕ (up to $\phi(t_{\text{CI}}) = -70.3^\circ$ in trajectory I-7; see Table 1), we may infer that it is mechanistically possible for photoexcited molecules within the confines of the crystal lattice to undergo a full twist around the C2–C3 bond and, in doing so, to relax to the *anti* isomer. In conclusion, it is predicted that a fraction of photoexcited molecules do isomerize to the *anti* form.

In what follows, we discuss in detail two representative simulated trajectories.

4.3.1. Trajectory II-5. Trajectory II-5 underwent proton transfer at $t = 80.5$ fs and subsequently reached the S_1/S_0 CI at $t = 335.5$ fs, at which point the simulation was discontinued.

In Figure 6a, we present a three-dimensional projection of trajectory II-5 onto energy, proton transfer, and proton donor–

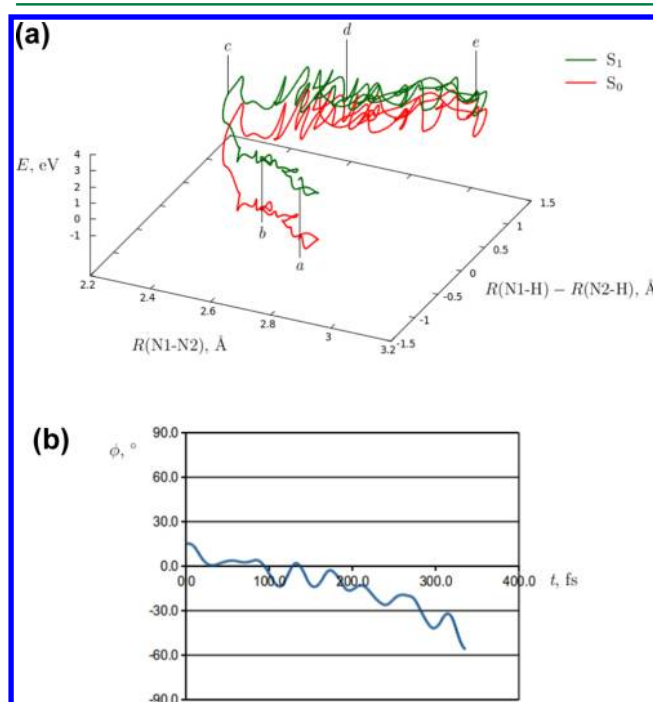


Figure 6. Trajectory II-5. (a) Projection of trajectory II-5 onto energy, proton transfer, and proton donor–acceptor distance coordinates. The potential energy of the photoexcited system and the ground-state energy calculated at the same geometry are plotted in green and red, respectively. The labels *a* to *e* are explained in the text. (b) Time evolution of torsion angle ϕ in trajectory II-5.

acceptor distance coordinates, which provides a comprehensive mechanistic description of the photochemical reaction. The projection can be roughly divided into a number of segments that correspond to specific events occurring along the trajectory; these are marked as *a* to *e* in Figure 6a. Point *a* is the starting point of the trajectory and corresponds to the photoexcited molecule in conformation *1-syn*. Segment *b* is largely parallel to the proton donor–acceptor distance coordinate, $R(\text{N1-N2})$, and corresponds to a shortening of the distance between the two nitrogen atoms before the proton transfer step. The next segment *c*, mostly parallel to the proton transfer coordinate, is the proton transfer step. The potential energy gap between the excited and ground states decreases by

around 1.5 eV during the proton transfer step *c*. Further along the trajectory, segment *d* corresponds to the relaxation of the molecule on the excited-state potential energy surface following proton transfer. Although segment *d* as a whole is mostly parallel to the coordinate $R(\text{N1}–\text{N2})$, its early part (near the juncture of segments *c* and *d*) exhibits strong oscillations along the proton transfer coordinate. These oscillations are caused by the vibrational excitation of the newly formed $\text{N2}–\text{H}$ bond immediately following proton transfer. It takes around 10 oscillation periods for these large-amplitude vibrations to be dampened out.

As seen in Figure 6b, where the torsion angle ϕ is plotted as a function of time, immediately after proton transfer at $t = 80.5$ fs, which occurred at a near-planar geometry, the photoexcited molecule started to undergo twisting motions that modulated the torsion angle ϕ . Through these motions, the pyridyl and indolyl moieties gradually rotated in opposite directions, until the photoexcited molecule reached the S_1/S_0 CI at $t = 335.5$ fs. The point at which the photoexcited molecule reached the S_1/S_0 CI is marked as *e* in Figure 6a.

The overall sequence of proton donor–acceptor distance shortening (*b*), followed by proton transfer at a near-planar geometry (*c*) and relaxation involving a lengthening of the donor–acceptor distance (*d*), and finally twisting motions ultimately leading to the S_1/S_0 CI (*e*) is shared by all simulated trajectories.

Finally, we turn our attention to the configuration of the simulated system in trajectory II-5 as it reached the S_1/S_0 CI. In Figure 7, the final frame from the trajectory, immediately before the CI is reached, is overlaid on the experimental crystal structure of 7PyIn. From this image, we can confirm that the S_1/S_0 CI is reached by the simultaneous twist of the pyridyl and

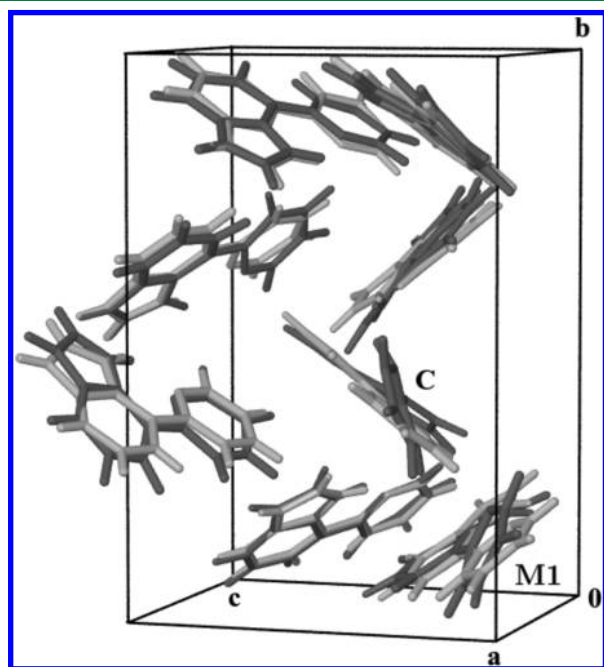


Figure 7. An overlay of the instantaneous configuration of the system on reaching the S_1/S_0 in trajectory II-5 and the experimental crystal structure of 7PyIn, drawn in dark gray and light gray, respectively. The photoexcited molecule is labeled C. M1 is a molecule neighboring C whose pyridyl moiety undergoes significant displacement from its crystallographic position during the simulated photoreaction. Unit cell axes *a*, *b*, and *c* shown.

indolyl moieties in opposite directions. A survey of other trajectories that reach the CI shows that the CI can be reached by torsion in either direction (that is to say, by torsion toward both more positive and more negative values of ϕ).

Visual inspection of trajectory II-5 reveals that concurrent with the twisting motion of the photoexcited molecule C, the indolyl moiety of a neighboring molecule (labeled M1 in Figure 7) becomes significantly displaced from its crystallographic position, away from molecule C (note that molecules C and M1 are neighbors because of the periodic boundary conditions imposed in order to simulate the crystal lattice). The displacements of the other ground-state molecules from their crystallographic positions are not greater in magnitude than typical thermal displacements within the ground-state system. While due to the low number of simulated trajectories it was not possible to rigorously study correlations between the twisting motion of the photoexcited molecule and the movements of the surrounding ground-state molecules, it seems plausible to surmise that in trajectory II-5 the displacement of molecule M1 is caused by the torsional motion of the photoexcited molecule C. Similar instances of molecules neighboring C becoming displaced from their crystallographic positions while C approaches the S_1/S_0 CI were observed in some other trajectories, including trajectory I-1 which will be reviewed in due course.

4.3.2. Trajectory I-1. In trajectory I-1, following proton transfer at $t = 55.5$ fs, the photoexcited molecule underwent torsion around the $\text{C2}–\text{C3}$ bond, and the criterion for the system reaching the S_1/S_0 conical intersection was met at $t = 184.5$ fs, at which point the simulation was terminated.

In Figure 8a, a projection is shown of the trajectory onto the energy, proton transfer, and proton donor–acceptor distance coordinates. Distinct proton donor–acceptor shortening and proton transfer steps of the trajectory can be identified (segments *b* and *c*, respectively). In the relaxation segment *d*, vibrational excitation of the $\text{N2}–\text{H}$ bond is again visible, although the amplitude of the oscillations is lower and they are dampened out more rapidly than in trajectory II-5. Finally, at point *e*, 184.5 fs after the initial photoexcitation, the photoexcited molecule reached the S_1/S_0 conical intersection. A plot of torsion angle ϕ as a function of time during trajectory I-1 is shown in Figure 8b. Before the termination of trajectory I-1, the photoexcited molecule reached a torsion angle ϕ of -58.0° , which represents the second highest absolute value of ϕ on reaching the S_1/S_0 CI from all 16 simulated trajectories.

In Figure 9, we present an overlay of the final frame from the trajectory and the experimental crystal structure of 7PyIn. Analogously to trajectory II-5, in trajectory I-5 one of the molecules neighboring the photoexcited molecule C, labeled M2 in Figure 9, appears to become significantly displaced from its crystallographic position at the same time that C undergoes twisting motions and approaches the conical intersection.

5. CONCLUSIONS

We have applied a novel implementation of the hybrid QM/QM simulation method to study the photochemical reaction of 7PyIn in the molecular crystal phase. Both the ESIPT step and the subsequent torsional skeletal deformation leading to an S_1/S_0 conical intersection are essentially barrierless. The ESIPT has been simulated to occur within 80 fs, on average, of the initiatory photoexcitation. By reaching the S_1/S_0 conical intersection, the photoexcited molecule is predicted to be able to undergo *syn* to *anti* photoisomerization.

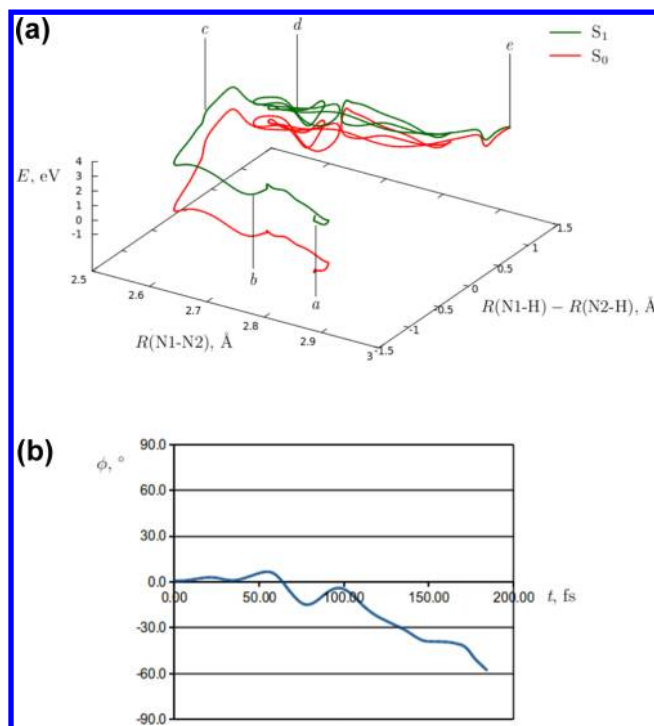


Figure 8. Trajectory I-1. (a) Projection of trajectory I-1 onto energy, proton transfer, and proton donor–acceptor distance coordinates. The potential energy of the photoexcited system, and the ground-state energy calculated at the same geometry, are plotted in green and red, respectively. The labels *a* to *e* are explained in the text. (b) Time evolution of torsion angle ϕ in trajectory I-1.

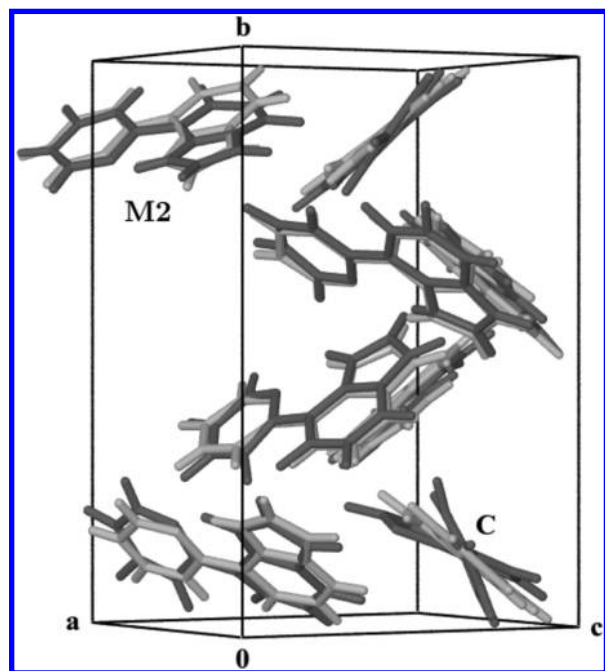


Figure 9. An overlay of the instantaneous configuration of the system on reaching the S_1/S_0 and the experimental crystal structure of 7PyIn, drawn in dark gray and light gray, respectively. The photoexcited molecule is labeled **C**. **M2** is a molecule neighboring **C** whose indolyl moiety undergoes significant displacement from its crystallographic position during the simulated photoreaction. Unit cell axes *a*, *b*, and *c* shown.

An unresolved issue is the correctness of the TD-DFT description of the potential energy of the S_1 state of the 7PyIn molecule along the torsional coordinate (ϕ). While utmost care has been exercised to take into account the possible error due to the use of the TD-DFT method during the analysis of simulated trajectories, the fact remains that the TD-DFT method was stretched to the limit when the photoexcited molecule approached the S_1/S_0 conical intersection. This, however, is part of the broader problem of efficient computer simulation of excited states and, as such, is beyond the scope of the present work. We wish to underline here that any suitable electronic structure method can be incorporated into the hybrid QM/QM method for the purpose of describing the photoexcited molecule, and therefore the QM/QM method itself is not encumbered by the inherent limitations of TD-DFT.

While at present no experimental data are available to verify the prediction made regarding the occurrence of *syn* to *anti* isomerization, it is in line with the well-established general relationship between the crystal structure and photoreactivity of a wide range of structurally similar Schiff bases. We hope that the present study will stimulate experimental research into the mechanistic details of ultrafast reactions taking place in the molecular crystal phase.

■ ASSOCIATED CONTENT

Supporting Information

Embedded cluster calculations. This material is available free of charge via the Internet at <http://pubs.acs.org>.

■ AUTHOR INFORMATION

Corresponding Author

*E-mail: C.Morrison@ed.ac.uk.

Notes

The authors declare no competing financial interest.

■ ACKNOWLEDGMENTS

M. A. Kochman gratefully acknowledges the University of Edinburgh and the Centre for Numerical Algorithms and Intelligent Software (NAIS) for the award of a Principal's Career Development Scholarship. Work made use of the EaSTCHEM Research Computing Facility (<http://www.eastchem.ac.uk/rcf>) and the Edinburgh Compute and Data Facility (ECDF) (<http://www.ecdf.ed.ac.uk/>). We would like to thank Prof. M. Paterson from the Institute of Chemical Sciences at Heriot–Watt University for fruitful discussions. We also wish to acknowledge the use of the EPSRC funded Chemical Database Service at Daresbury.

■ REFERENCES

- (1) Gütllich, P.; Hauser, A.; Spiering, H. *Angew. Chem., Int. Ed. Engl.* **1994**, *33*, 024–2054.
- (2) Irie, M.; Kobatake, S.; Horichi, M. *Science* **2001**, *291*, 1769–1772.
- (3) Al-Kaysi, R. O.; Bardeen, C. J. *Adv. Mater.* **2007**, *19*, 1276–1280.
- (4) Nakatani, K.; Delaire, J. A. *Chem. Mater.* **1997**, *9*, 2682–2684.
- (5) Park, S.; Kwon, O.-H.; Kim, S.; Park, S.; Choi, M.-G.; Cha, M.; Park, S. Y.; Jang, D.-J. *J. Am. Chem. Soc.* **2005**, *127*, 10070–10074.
- (6) Narasimha Moorthy, J.; Mal, P.; Natarajan, R.; Venugopalan, P. *J. Org. Chem.* **2001**, *66*, 7013–7019.
- (7) MacGillivray, L. R. *J. Org. Chem.* **2008**, *73*, 3311–3317.
- (8) Toda, F. *Acc. Chem. Res.* **1995**, *28*, 480–486.
- (9) Scheffer, J. R.; Xia, W. *Top. Curr. Chem.* **2005**, *254*, 233–262.
- (10) Kimmel, A. V.; Ramo, D. M.; Sushko, P. V.; Shluger, A. L.; Kuklja, M. M. *Phys. Rev. B* **2009**, *80*, 134108.

- (11) Warshel, A.; Shakked, Z. *J. Am. Chem. Soc.* **1975**, *97*, 5679–5684.
- (12) Basilevsky, M. V.; Tikhomirov, V. A. *Mol. Phys.* **2008**, *106*, 2391–2405.
- (13) Sobolewski, A. L.; Domcke, W. *J. Phys. Chem. A* **2007**, *111*, 11725–11735.
- (14) Aquino, A. J. A.; Plasser, F.; Barbatti, M.; Lischka, H. *Croat. Chem. Acta* **2009**, *82*, 105–114.
- (15) Barbatti, M.; Aquino, A. J. A.; Lischka, H.; Schriever, C.; Lochbrunner, S.; Riedle, E. *Phys. Chem. Chem. Phys.* **2009**, *11*, 1406–1415.
- (16) Ortiz-Sánchez, J. M.; Gelabert, R.; Moreno, M.; Lluch, J. M. *J. Chem. Phys.* **2008**, *129*, 214308.
- (17) Nosenko, Y.; Wiosna-Salyga, G.; Kunitski, M.; Petkova, I.; Singh, A.; Buma, W. J.; Thummel, R. P.; Brutschy, B.; Waluk, J. *Angew. Chem., Int. Ed.* **2008**, *47*, 6037–6040.
- (18) Sténson, P. *Acta Chem. Scand.* **1970**, *24*, 3729–3738.
- (19) Taneda, M.; Kodama, Y.; Eda, Y.; Koyama, H.; Kawato, T. *Chem. Lett.* **2007**, *36*, 1410–1411.
- (20) Bregman, J.; Leiserowitz, L.; Osaki, K. *J. Chem. Soc.* **1964**, 2086–2100.
- (21) Hadjoudis, E.; Mavridis, I. M. *Chem. Soc. Rev.* **2004**, *33*, 579–588.
- (22) Johmoto, K.; Ishida, T.; Sekine, A.; Uekusa, H.; Ohashi, Y. *Acta Crystallogr.* **2012**, *B68*, 297–304.
- (23) Wanko, M.; Garavelli, M.; Bernardi, F.; Niehaus, T. A.; Frauenheim, T.; Elstner, M. *J. Chem. Phys.* **2004**, *120*, 1674–1692.
- (24) Mudadu, M. S.; Singh, A.; Thummel, R. P. *J. Org. Chem.* **2006**, *71*, 7611–7617.
- (25) Fletcher, D. A.; McMeeking, R. F.; Parkin, D. J. *Chem. Inf. Comput. Sci.* **1996**, *36*, 746–749.
- (26) Warshel, A.; Levitt, M. *J. Mol. Biol.* **1976**, *103*, 227–249.
- (27) Senn, H. M.; Thiel, W. *Top. Curr. Chem.* **2007**, *268*, 173–290.
- (28) Bernstein, N.; Kermode, J. R.; Csányi, G. *Rep. Prog. Phys.* **2009**, *72*, 026501.
- (29) Bearpark, M. J.; Larkin, S. M.; Vreven, T. *J. Phys. Chem. A* **2008**, *112*, 7286–7295.
- (30) Altoè, P.; Stenta, M.; Bottoni, A.; Garavelli, M. *Theor. Chem. Acc.* **2007**, *118*, 219–240.
- (31) Santos, H. R. R.; Ramos, M. J.; Gomes, J. A. N. F. *Phys. Rev. B* **2005**, *72*, 075445.
- (32) Tuma, C.; Sauer, J. *Phys. Chem. Chem. Phys.* **2006**, *8*, 3955–3965.
- (33) Handzlik, J. *Int. J. Quantum Chem.* **2007**, *107*, 2111–2119.
- (34) Hansen, N.; Brüggemann, T.; Bell, A. T.; Keil, F. J. *J. Phys. Chem. C* **2008**, *112*, 15402–15411.
- (35) Svelle, S.; Tuma, C.; Rozanska, X.; Kerber, T.; Sauer, J. *J. Am. Chem. Soc.* **2009**, *131*, 816–825.
- (36) Lundberg, M.; Sasakura, Y.; Zheng, G.; Morokuma, K. *J. Chem. Theory Comput.* **2010**, *6*, 1413–1427.
- (37) Hratchian, H. P.; Krukau, A. V.; Parandekar, P. V.; Frisch, M. J.; Raghavachari, K. *J. Chem. Phys.* **2011**, *135*, 014105.
- (38) Adamo, C.; Barone, V. *J. Chem. Phys.* **1999**, *110*, 6158–6169.
- (39) Frisch, M. J.; Trucks, G. W.; Schlegel, H. B.; Scuseria, G. E.; Robb, M. A.; Cheeseman, J. R.; Scalmani, G.; Barone, V.; Mennucci, B.; Petersson, G. A.; Nakatsuji, H.; Caricato, M.; Li, X.; Hratchian, H. P.; Izmaylov, A. F.; Bloino, J.; Zheng, G.; Sonnenberg, J. L.; Hada, M.; Ehara, M.; Toyota, K.; Fukuda, R.; Hasegawa, J.; Ishida, M.; Nakajima, T.; Honda, Y.; Kitao, O.; Nakai, H.; Vreven, T.; Montgomery, J. A., Jr.; Peralta, J. E.; Ogliaro, F.; Bearpark, M.; Heyd, J. J.; Brothers, E.; Kudin, K. N.; Staroverov, V. N.; Kobayashi, R.; Normand, J.; Raghavachari, K.; Rendell, A.; Burant, J. C.; Iyengar, S. S.; Tomasi, J.; Cossi, M.; Rega, N.; Millam, J. M.; Klene, M.; Knox, J. E.; Cross, J. B.; Bakken, V.; Adamo, C.; Jaramillo, J.; Gomperts, R.; Stratmann, R. E.; Yazyev, O.; Austin, A. J.; Cammi, R.; Pomelli, C.; Ochterski, J. W.; Martin, R. L.; Morokuma, K.; Zakrzewski, V. G.; Voth, G. A.; Salvador, P.; Dannenberg, J. J.; Dapprich, S.; Daniels, A. D.; Farkas, Ö.; Foresman, J. B.; Ortiz, J. V.; Cioslowski, J.; Fox, D. J. *Gaussian 09*, revision A.02; Gaussian, Inc.: Wallingford, CT, 2009.
- (40) Frisch, M. J.; Trucks, G. W.; Schlegel, H. B.; Scuseria, G. E.; Robb, M. A.; Cheeseman, J. R.; Montgomery, J. A., Jr.; Vreven, T.; Kudin, K. N.; Burant, J. C.; Millam, J. M.; Iyengar, S. S.; Tomasi, J.; Barone, V.; Mennucci, B.; Cossi, M.; Scalmani, G.; Rega, N.; Petersson, G. A.; Nakatsuji, H.; Hada, M.; Ehara, M.; Toyota, K.; Fukuda, R.; Hasegawa, J.; Ishida, M.; Nakajima, T.; Honda, Y.; Kitao, O.; Nakai, H.; Klene, M.; Li, X.; Knox, J. E.; Hratchian, H. P.; Cross, J. B.; Bakken, V.; Adamo, C.; Jaramillo, J.; Gomperts, R.; Stratmann, R. E.; Yazyev, O.; Austin, A. J.; Cammi, R.; Pomelli, C.; Ochterski, J. W.; Ayala, P. Y.; Morokuma, K.; Voth, G. A.; Salvador, P.; Dannenberg, J. J.; Zakrzewski, V. G.; Dapprich, S.; Daniels, A. D.; Strain, M. C.; Farkas, Ö.; Malick, D. K.; Rabuck, A. D.; Raghavachari, K.; Foresman, J. B.; Ortiz, J. V.; Cui, Q.; Baboul, A. G.; Clifford, S.; Cioslowski, J.; Stefanov, B. B.; Liu, G.; Liashenko, A.; Piskorz, P.; Komaromi, I.; Martin, R. L.; Fox, D. J.; Keith, T.; Al-Laham, M. A.; Peng, C. Y.; Nanayakkara, A.; Challacombe, M.; Gill, P. M. W.; Johnson, B.; Chen, W.; Wong, M. W.; Gonzalez, C.; Pople, J. A. *Gaussian 03*, revision E.01; Gaussian, Inc.: Wallingford, CT, 2004.
- (41) Perdew, J. P.; Burke, K.; Ernzerhof, M. *Phys. Rev. Lett.* **1996**, *77*, 3865–3868.
- (42) Clark, S. J.; Segall, M. D.; Pickard, C. J.; Hasnip, P. J.; Probert, M. I. J.; Refson, K.; Payne, M. C. *Z. Kristallogr.* **2005**, *220*, 567–570.
- (43) Materials Studio CASTEP Online Help. H_00PBE.usp uses one valence electron (s state), C_00PBE.usp uses four valence electrons (s and p state), and N_00PBE.usp uses five valence electrons (s and p state).
- (44) Grimme, S. *J. Comput. Chem.* **2006**, *27*, 1787–1799.
- (45) Lochbrunner, S.; Wurzer, A. J.; Riedle, E. *J. Phys. Chem. A* **2003**, *107*, 10580–10590.
- (46) Schriever, C.; Lochbrunner, S.; Ofial, A. R.; Riedle, E. *Chem. Phys. Lett.* **2011**, *503*, 61–65.